RENDERING THREE DIMENSIONAL

SOLAR CORONAL STRUCTURES

G. ALLEN GARY

Space Sciences Laboratory/ES82

George C. Marshall Space Flight Center/NASA

Huntsville, AL 35812, U.S.A.[1]

*Received*_____

*Revised*_____

Running Head: Solar Coronal Structures

[1] E-mail: Allen.Gary@msfc.nasa.gov

Abstract. An X-ray or EUV image of the corona or chromosphere is a 2D representation of an extended 3D complex for which a general inversion process is impossible. A specific model must be incorporated in order to understand the full 3D structure. We approach this problem by modeling a set of optically-thin 3D plasma flux tubes which we render these as synthetic images. The resulting images allow the interpretation of the X-ray/EUV observations to obtain information on (1) the 3D structure of X-ray images, i.e., the *geometric* structure of the flux tubes, and on (2) the internal structure using specific plasma characteristics, i.e., the *physical* structure of the flux tubes. The data-analysis technique uses magnetograms to characterize photospheric magnetic fields and extrapolation techniques to form the field lines. Using a new set of software tools, we have generated 3D flux tube structures around these field lines and integrated the plasma emission along the line of sight to obtain a rendered image. A set of individual flux-tube images is selected by a non-negative least squares technique to provide a match with an observed X-ray image. The scheme minimizes the squares of the differences between the synthesized image and the observed image with a non-negative constraint on the coefficients of the brightness of the individual flux-tube loops. The derived images are used to determine the specific photospheric foot points and physical data, i.e., scaling laws for densities and loop lengths. The development has led to computer efficient integration and display software that is compatible for comparison with observations (e.g., *Yohkoh* SXT data, NIXT, or EIT). This analysis is important in determining directly the magnetic field configuration, which provides the structure of coronal loops, and indirectly the electric currents or waves, which provide the energy for the heating of the plasma. We have used very simple assumptions (i.e., potential magnetic fields and isothermal corona) to provide an initial test of the techniques before complex models are introduced. We have separated the *physical* and *geometric* contributions of the emission for a set of flux tubes and concentrated, in this initial study, on the *geometric* contributions by making approximations to the physical contributions. The initial results are consistent with the scaling laws derived from the *Yohkoh* SXT data.

Subject Headings: Sun: magnetic fields, Sun: coronal loops

1. Introduction

1.1 HISTORICAL BACKGROUND

As a historical introduction to the subject of rendering solar magnetic structures, we note that using magnetic field extrapolations to infer the 3-dimensional (3D) structure of coronal loops started with the computer code devised by Schmidt in the early 1960's (Schmidt 1965; Harvey 1966, Harvey 1969, Schmidt 1964). Rust was the first to use Schmidt's extrapolation scheme to compare the 3D magnetic field structure with the coronal loops (Rust, 1966; Rust and Roy, 1971; Rust, 1970). At the Crimean Astrophysical Observatory a similar code was developed by Godovnikov and Smirnova (Godovnikov and Smirnova, 1965). Rust's comparisons showed a good correlation of the current-free field lines with the direction of the coronal loop structures. The set of field lines closely matched the observations at the limb, even though there was a time delay between the H_α observation and the magnetogram. The good correlation was accomplished, in part, by eliminating regions which showed substantial evolution. The result of this study was a confirmation of potential-like configurations of the coronal loops in terms of position, orientation, and height. However, nothing was stated concerning the line-of-sight effects, even though, in these limb observations, the brightening at the loop tops were used implicitly to set the heights of the field-line extrapolations. The brightenings are obviously the results of line-of-sight effects. In this paper we will develop a specific treatment of the coronal X-ray structures by synthesizing line-of-sight images of an optically thin plasma for comparison with observations.

The coronal loops were observed in prominences in the 1860's and Fox photographed and described them in 1908 (Fox 1908, Bray et al. 1991). It was the spectrographs at Yerkes and Mt. Wilson Observatories that allowed Fox, Pettit, Ellison, and Hale to analyze the prominences, and it was the birefringent filter that allowed Lyot to photograph the fine scale loop structures. Such detailed observations of H_α loops, with the introduction of photoelectric magnetographs in the 1950-1960's, led Rust to his study.

The introduction of X-ray observations from rockets, *Skylab* and *SMM* allows analysis of the field-line extrapolations with these observations (Webb 1981; Sheeley et al. 1975; Hoyng et al 1981.; Poletto et al. 1975; Levine 1976). The analysis of soft X-ray images from *Skylab* in terms of quasi-static coronal loops leads to a set of scaling laws relating the maximum temperature, base pressure, and length of the loops (Rosner, Tucker and Vaiana 1978). Within the more recent *Yohkoh* observations, scaling law analysis continues to be refined giving better statistics in relating density, pressure, and arclength of loops (Reale and Peres 1995; Ciaravella et al. 1996; Kano and Tsuneta 1995; Yoshida and Tsuneta 1996). The present approach discussed herein extends the previous analyses by forming images for comparison with observations using scaling laws relationships. The resulting image of a set of potential flux tubes for an active region which best represents the soft X-ray observations determines a 3D model for the region.

The method here employs both physical and geometric data. Using such an approach, we will overcome the problem that the locations of the loop foot points are difficult to identify (Yoshida and Ogama 1995). The uncertainty of the loops' lengths would be of the order $>\pm 0.9 \times 10^{3}$km (Kano and Tsuneta 1995), which can lead to an uncertainty in the derived scaling law parameters. Although lower temperature sensitive observations can improve the foot point locations, one cannot follow the coronal loops to the photosphere (i.e., the "foot-a-sphere") (Yoshida et al. 1995). Determining the foot points is only one example of the usefulness of the general approach described here, i.e., matching the coronal structures to specific points in the photosphere via the potential extrapolation. Specifically, the comparison of the synthesized images and observations identifies the appropriate field lines through which the foot points can be determined. As we shall show, the development of a flux-tube image technique provides a much deeper insight into the 3D structures of the corona.

1.2 APPROACH

The approach used is to employ a *magnetic model*: either a potential or force-free magnetic field extrapolation of a magnetogram to obtain a set of 3D magnetic field lines. Having these field lines, the *geometry model* for the flux tubes is defined by a set of vertices which are generated by using the conservation of flux. These flux tubes are filled with an optically thin plasma as given by a specific *physical model* of the plasma and the flux-tube images of these are produced by an *imaging technique*. With a set of individual coronal flux-tube images, a positive linear combination is constructed into a soft X-ray image in order to assign the particular emission characteristic to each flux tube when compared with observations. This *inversion technique* employs a nonnegative least squares approach. Such analysis provides a much better understanding of the strengths and weaknesses of the specific models and parameters used in creating the field lines and the physical characteristics of the flux tubes. We have emphasized the geometric contribution in this paper, as compared to Alexander and Katsev (1996) , who recently studied the problem emphasizing the physical component.

Out of such an analysis the parameters and the assumptions for the various magnetic, geometric, and physical models can be pursued. The approach will help to answer questions such as: Where are the specific foot points in the photosphere for the heated X-ray flux tubes and what is unique about these photospheric regions? What are the specific emission features and temperatures for the X-ray loops? What is the volume filling factors for the heated X-ray loops? What is the nature of the diffuse background fog associated with the active regions? What contributions are the nonpotential, nonforce-free magnetic fields near the photosphere? What is the model for the specific excitation channels from the photosphere to the corona?

Because of the historical use of field lines in comparing the magnetic structure with the observed topology of observational images, we will first start with some appropriate comments of their use and some new findings using them (Section 2.1). Also as a preamble to the full treatment of transparent flux tubes which uses optical thin flux tubes, we will show a view of field lines with their "solid" flux tubes drawn (Section 2.2). This immediately draws attention to the expansion of the flux tube with height. Then the main emphasis of the paper is presented with the method of rendering the soft X-ray flux tubes and the inversion technique which is used to determine the

relative emission strength of the individual flux tubes (Section 3.0) . With the assistance of the appropriate scaling laws, these relative strengths are then used to obtain a set of physical parameters for each flux tube (Section 4.0). For example, having the length and equating the emission factor to brightness of the loop, we can obtain a scatter diagram consistent with the scaling laws.

2. Representations

2.1 FIELD LINES

 Field-line configurations provide a unique analysis method to derive information from solar magnetograms. The field-lines configurations have been used to determine the consistency and interconnection of the photospheric and chromospheric magnetic fields. The early extrapolations of magnetograms used current-free fields situated about active regions (Schmidt 1965; Semel 1967). As stated above, the agreement between the chromospheric linear features and the photospheric field extrapolations were generally good for potential-like fields. Nakagawa (Nakagawa 1973; Nakagawa and Raadu1972; Nakagawa et al. 1971; Raadu and Nakagawa 1971; Wellck and Nakagawa 1973) and Levine (Levine 1975; Levine1976; Levine and Altschuler 1977) studied linear force-free fields for highly nonpotential regions and showed some consistency for these fields for a few active regions. Then Mikic and Wu and others (Mikic, Barnes, and Schnack 1988, Mikic, Schnack, and Van Hoven 1989,1990, Mikic and McClymont 1994; Roumeliotis 1994; Wu, Chang and Hagyard 1985; Wu et al. 1990; Wu and Sakurai 1990, Gary 1992) developed force-free extrapolations using vector magnetograms with some success. Because, in highly sheared regions the extrapolated potential field deviates from the observed transverse field, Hagyard and others (Hagyard 1988; Hagyard 1990; Moore, Hagyard and Davis 1987, Wang 1992) have detailed these differences in the shear analyses, which used extrapolated transverse potential field in comparison with the observed transverse field. P. Démoulin and others (Démoulin et al. 1994; Démoulin et al. 1993; Somov 1992) have employed the magnetic field extrapolations to determine the separators and separatrices to determine the places within active region complexes where reconnection can occur. Then the field extrapolations have been used in (1) the mapping of the connectivity of field lines, (2) the study of magnetic separators and separatrices, (3) the study of 3D topological structures in large scale coronal features (e.g., hairy-ball models), (4)   the comparison with potential and force-free fields, and (5) MHD modeling.

   There is yet a great deal to be learned about the 3D structures of coronal fields. Moreover, there is one area which has almost been overlooked that can contribute to the analysis of the solar magnetic configurations, in particular to the analysis of high resolution SXT images from *Yohkoh*. This is the area of image analysis which extends the field-line analysis.

  As an introduction to 3D image analysis, Klimchuk has analyzed a set of coronal loop images from SXT for cross-sectional properties (Kimchuk 1995; Klimchuk et al.1992) with extension by McClymont and Mikic (1994). We review Klimchuk's work here since it provides a transition between field-line analysis and the 3D rendering analysis presented later. It also shows, using potential flux tubes, that the analysis is consistent with the basic assumptions to be employed. His

summary observations were: (1) flux tubes have circular cross sections, (2) filled flux tubes have approximately uniform density cross sections, (3) cross sectional radii are similar for all loops, and (4) cross sectional radii of each loop are approximately constant. The conclusions (3) and (4) are consistent with the results from potential field-line calculations as shown in Figures 1 and 2. The data in these figures are associated with Active Regions 7645 and 7646/7647 on 1994 January 4. The coronal field lines were generated using Sakurai's potential code (Sakurai 1981) for spherical geometry and using the KPNO magnetogram of 1631UT (see Fig 1.). In Figure 2a the flux-tube ratio of radii, R, normalized to the apex value is plotted vs the normalized distance from the apex of each loop. Most of the field lines have a ratio between 1.0 and 0.25. The 60 representative field lines were selected by the strength of flux distribution algorithm for foot-point selection. The field lines with a R > 0.5 at the end of the loop are very short loops which can be identified in Figure 2b. In Figure 2b the inverse ratio of the radii, R^{-1}, is plotted vs the arclength from apex in units of Mm. In both plots of Figure 2, the radii are derived using the conservation of magnetic flux, i..e., $r/r_o = (B/B_o)^{-1/2}$, i.e. using the simple "microscopic" definition (McClymont and Mikic 1994). (For the average R an empirical model $R = \exp(-kR(\cos(\pi L/2)-1)$ can be given, where R is the radius of some representative circular loop and $k \sim 2/R$ is the vertical scale height for an exponentially decreasing magnetic field.) It is seen from Figures 2a and 2b that over more than 75 per cent of the length of the field line, the radius changes less than a factor or 2. McClymont and Mikic (1994) in an re-analysis of Klimchuk's observations used a force-free field extrapolation and used the 85 per cent point as their "foot point". Hence, using their results and considering the aspect ratio of the flux tubes, the potential field data of Figure 2 are consistent with Klimchuk's fourth observation, especially considering that SXT images are not sensitive to temperatures lower than ~2.5 MK, i.e., *the lower section of the legs are not seen*, and the force-free field analysis. For this nearly-potential transequatorial complex considered here, there is no need to consider the force-free field arguments imposed by McClymont and Mikic (1994). Apparently, the current systems in this complex are negligible.

The SXT images of active regions as seen on the limb of the sun (e.g., Fig.3, Tsuneta 1996) show that there is a preferred mean height for the distinguishable coronal structures. This is related to the scale height of the loops. This mean height would imply a fairly consistent radius, which is consistent with Klimchuk's third observation, if we assume results of Figure 2 (also see section 2.2 below).

We also note that the circular cross section implies that the observed line-of-sight path through the flux tubes is $\ell = 2(h(2h-R))^{1/2}$ as seen perpendicular to the longitudinal axis, where h is the distance of the line-of-sight path from the edge of the flux tube of radius R. Hence at $\ell = R$, $h = R(1-(3/4)^{1/2}) = 0.13$, and, hence, only at the edge, the last 13% of the cross section, does the intensity profile (ℓ) change by an additional factor of 2. Hence, Klimchuk's first observation (1) implies his observation (2). His analysis of images provides some important points, although consistent with potential fields, and provides a prelude and impetus to further image analysis.

2.2 SOLID FLUX TUBE

We have employed the flux-tube radii with the field-line calculations above. It is instructive to see the field-line plots with the associated flux tubes shown explicitly. In Figure 3 we have plotted the flux tubes associated with the same data set as Figures 1 and 2, keeping the base radius r_o constant. It is obvious that the higher reaching flux tubes have larger radii, which is a result of the lower associated field strength at the apex regions of these loops. If one mentally extracts the set of the very high flux tubes and selects only the remaining ones with approximately the same height, then the same diameters are seen, viz $r/r_o = (B/B_o)^{-1/2}$ and are consistent with observation. Also, if the lower legs of the flux tubes are removed, as they would be in soft X-ray images due to the lack of emission at the lower chromospheric temperatures, the cross sectional radii of each loop would be approximately constant.

We now will consider flux tubes which are physically more relevant, i.e., optically thin flux tubes.

2.3 RENDERING OPTICALLY THIN FLUX TUBES

A thin coronal magnetic flux tube or loop is here defined by a bundle of exterior field lines connecting two compact photospheric areas of opposite magnetic polarity, such that all interior field lines pass through both end regions. Each end region is simply connected. (Generally, the central interior field line of a flux tube is considered when one draws only field lines.) Hence, flux tubes are separate, slender tubes of small cross sections in which the enclosed plasma is relatively isolated by the magnetic field (Parker 1979 p.123; Bray et al.1991, p.262; Priest 1982, p. 108).

Observationally, loop-like structures have been observed during eclipses and with coronagraphs, heliospectrographs, EUV and X-ray telescopes, and are classified as open/closed hot/cool loops (Webb 1981). Hence, the earlier work by Rust (1966) and a continued process through *Skylab*, *SMM*, and *Yohkoh* eras have developed the consistent picture of the connection between the coronal loops and the observed coronal structures. We will now consider how to render these quasi-static hot, closed coronal loops that make up the majority of features seen in a soft X-ray image. However besides the individual loops, there is also an overall faint, diffuse emission associated with active regions. This diffuse emission could be related to (1) unresolved multi-loops heated by a basal process or/and (2) the point spread function of the X-ray telescopes. The effect of the point spread function of the Skylab X-ray imaging instruments is apparent when those images are compared to the Yohkoh/SXT images. For the SXT images, the faint, diffuse emission only reduces the contrast of the individual recognized loops, and is not considered here, but should be addressed in a detailed analysis.

The basic property of the flux tube is that the magnetic flux is conserved along the flux tube, $\nabla \cdot \mathbf{B} = 0$. The flux tube is not required to have a circular cross section, but we have assumed a circular cross section which is consistent with a uniform pressure distribution within the loop. Hence, if the base radius is r_o and the base field strength is B_o, then the radius of the flux tube

behaves as $r=r_o(B/B_o)^{1/2}$. In using this approach we assume that the flux tube is thin, i.e., no flux tube expands into an adjacent flux tube. If we start at the, say, foot point of positive longitudinal field with a circular cross section for the flux tube, then the derivation from a circular cross section is dependent on the distribution of the field lines at the other (negative) foot point. The correction for non-circular flux tubes can be made using a set of field lines; this correction has not been applied in the results presented here. The correction would be to establish the flux tube geometry by using a set of foot points defining a circular cross section at *only* one end of the flux tube and following the associated field lines to the other foot point.

 We ignore the small confining current for the flux tubes, i.e., we assume that the magnetic field produced by the confining current is much a weaker than the field defining the field lines. Hence the field-extrapolation procedure will not have to produce the confinement current. Hence, it is assumed that the dominating field is a potential field and the flux tubes with different pressures and temperatures can coexist by small currents about the flux tubes which are not drastically changing the global potential field configuration, i.e., $\Delta p << B^2/8\pi$.

Furthermore, we will assume quasi-static equilibrium. Since Lorentz forces vanish in the direction of the magnetic field, identically $\mathbf{B}\cdot(\mathbf{j}\times\mathbf{B})=0$, and the force balance equation leads to hydrostatic equilibrium along the field line: $\mathbf{B}\cdot(-\nabla p+ \rho\nabla\Phi)=0$. Then, following Bray et al. (1991, p.289), the pressure along a particular field line is given by

$$p = p(0)\, e^{-\int \frac{1}{\Lambda(\zeta)} d\zeta} ,$$

where $\Lambda(z)$ is the pressure scale height at z, and

$$\Lambda(z) = \frac{kT(z)}{\mu\, m_H\ \left[g_s R_s^2 / (R_s + z)^2\right]} .$$

The scale height is between 50 Mm $< \Lambda <$ 200 Mm for $0 < z < R_s$ and for a canonical coronal temperature of $T\sim 2\times 10^6$ K. The scale height Λ and the maximum z for a coronal loop, z_{max}, are such that $z_{max}/\Lambda \leq 1$, and the electron number density shows generally little variation along an isothermal portion of a flux tube,

$$\frac{N_e(R_s + z)}{N_e(R_s)} = e^{-\frac{z}{\Lambda}\left(\frac{R_s+z}{R_s}\right)} ,$$

where $N_e = \pi \rho/ \mu\, m_H$. We will assume the loops being rendered are in isothermal hydrostatic equilibrium.

 The thermal plasma emission spectrum has been calculated in detail (e.g. Mewe et al. 1985, 1986). In general, thermal bremsstrahlung accounts for the shape of the soft X-ray emission. When broadband filters are employed , the inclusion of the line emissions does not change the general shape of the emission profile, but specific calculations can be preformed to account for these lines.. The thermal free-free bremsstrahlung emission flux, j_λ, per unit volume per steradian per wavelength interval is given in the first order by simply

$$j_\lambda = 10^{-27.77}\, \frac{g(T_6,\lambda)}{T_6^{1/2}\, \lambda^2}\, N_e\, N_i\, e^{-\frac{hc}{\lambda kT}} \quad \text{erg s}^{-1}\ \text{cm}^{-3}\ \text{Å}^{-1}\ \text{sr}^{-1},$$

where N_i is the number density of ions and g is the Gaunt factor which is ~1 for the corona (Culhane 1969; Elwert 1961; Gibson 1973; Lang 1980; Maggio and Peres 1996). This emission distribution maximizes at $\lambda = 72/T_6$ Å. Since $hc/\lambda kT \sim 1$ and $N_e = N_i$, then $j_\lambda \sim N_e^2/T^{1/2}$, and if the corona is assumed isothermal, then the emission is related to the square of the density $j_\lambda \sim N_e^2$.

For the purpose of rendering the magnetic flux tubes, the response to the soft X-rays from free-free emission can be any simple response curve since we will assume an isothermal plasma. With the additional complexity, the thermal spectrum of Mewe et al. (1985,1986) could be combined with the X-ray instrument response curves (e.g., *Yohkoh* SXT Operation Manual 1992).

Alternatively, we could improve the thermal emission model by introducing the remarkably robust scaling laws. However, in the present paper we will derive the associated relationships with the scaling laws. These models can be determined by selecting any two parameters from p_o, L, T_{max}, or E_H, where p_o is the base pressure, L is the loop's semi-length, T_{max} is the maximum temperature at the top of the loop, and E_H is the heating per unit volume. Following Serio et al. (1981) and A. Maggio and G. Peres (1996), these quantities are linked by the scaling laws:

$$T_{max} = 1.4 \times 10^3 \left(p_o\, L\right)^{1/3} e^{\frac{-0.04 L}{\Lambda^*}},$$

$$E_H = 10^5\ p_o^{7/6}\ L^{-5/6}\ e^{\frac{-0.05 L}{\Lambda^*}},$$

where $\Lambda^* = 2kT/\mu m_{Hg}^*$ is the pressure scale height evaluated at the loop apex (Ciaravella et al. 1996; Maggio and Peres 1996). Assuming uniform pressure and heating rates along the loop, the analytic solution relating arclength s and temperature T along the loop is

$$s(T) = s(T_o) + \frac{2.5 \times 10^5}{p_0}\left[9.6 \times 10^{-16}\ T_{max}^3\ f\left(T, T_{max}\right) + 1\right],$$

where $f(T,T_{max}) = \arcsin(T/T_{max}) - (T/T_{max})(1-(T/T_{max})^2)^{1/2}$ and $T_o = T(s=0) \sim 2 \times 10^4$ K (Rosner, Tucker and Vaiana 1978). However, over a majority of the loop the temperature is ~T_{max} (e.g., see Fig. 2 in Serio et al 1981; Reale and Peres1995). The scaling law is insensitive as to how the heat is deposited along the loop (Kano and Tsuneta 1995). The scaling law may be different for transient and quasi-steady loops (Shimizu 1994; Shimizu et al. 1994; Kano and Tsuneta1995). Hence, the results presented here may have wide scatter plots due to the effect of having some non-stable loops included.

Significantly, the 3D emission pattern from a flux tube can be separated into the *physical* and *geometric* contributions. The physical part depends on the internal plasma structure of the flux tube - the thermal emissivity, temperature, density of electrons and ions, etc. For the *Yohkoh* observations, the temperature can be obtained from the SXT multi-filter observations. However, for this initial study we will fix the free parameters of the physical contribution part of the flux-tube models and consider only the geometric contributions. This is due to the approximation of the isothermal nature of each individual flux tube, hence the density dependency will be related to the emission strength of the overall value of the individual flux tube. The geometric part depends on the line-of-sight integration through the flux tube. Using a set of field-line data given by the field strength **B**(s) and the coordinate **r**(s) along the field line and a base radius of r_o, we can construct a circular flux tube in three dimensions, as per Figure 3.

Since the physical condition of steady coronal loops depends only on the local heating deposition within the loops and is determined *independently* of the neighboring loops, this implies that the steady coronal loops with various temperatures and pressures are isolated entities of the solar corona (Kano and Tsuneta 1995). Therefore, the 2D rendering of a coronal loop, when the physical contribution is constant, for each individual flux tube, results in determining only the line-of-sight segment within the flux tube. The solution of this plasma-volume rendering problem is to define the set of voxels which defines the flux tube. Having these voxels, we can assign to each voxel (a cubic volume element) a numerical value of the emissivity of the contained plasma. We redefine the coordinate system by rotating the coordinates so that we have a new z-axis co-linear with the line-of-sight direction. Then to define the "brightness" contribution for each image-plane pixel, we collapse the line-of-sight contributions by summing the voxels in the new z-direction to obtain a 2D image of the flux tube for a specific "look" direction (see Drebin, Carpenter, and Hanrahan (1988) for a discussion of the voxel technique). We assume an optically thin plasma with ignorable opacity.

Having the field lines, the main geometric problem in computational-volume rendering is how to specify the volume occupied by the voxels when one generates the line-of-sight paths. The continuous 3D space, R^3, is replaced by discrete 3D voxel-space Z^3 of an array of points. The solution we use is a nearest-neighbor volume-rendering technique. An entire volume (a cubic frame buffer) containing a flux tube is divided into small voxels, i.e., an array of voxel tessellates Z^3. Each voxel contains a coordinate-defining index (i,j,k). One foot point of the flux tube longitudinal axis defines the starting voxel for the search. All surrounding voxels are checked to determine if they are within the flux tube. We check the six direct neighbors (face neighbors) and the twelve indirect neighbors (edge neighbors), but the eight remote neighbors (corner neighbors) are not checked since we are dealing with an extended flux tube (Kaufman, 1987). The contiguous voxels within the flux tubes are mapped out. This scheme avoids investigating the entire volume and only a "skin" of voxels around the flux tube is explored unnecessarily. Having these voxels the 2D rendering is straight forward, e.g. in IDL reference the library programs project_vol or voxel_proj (see Figures 4 and 5). The Interactive Data Language (IDL) (@Research Systems, Inc.) is employed on a Silicon Graphics SGI 4D/480 RE Power Series computer for both the rendering and non-negative least squares inversion routine.

3.0 Inversion Techniques

3.1 BASIS FUNCTIONS

The mathematical basis of forming the images and selecting the appropriate coefficients is discussed in this section. If we form images with m×m pixels, then each image and any linear combination can be considered as a vector of m^2 elements. Using a set of individual loop images {f}, we define a finite-dimensional linear sub-space using the linear combination

$$V \;=\; \alpha_1 f_1 + \alpha_2 f_2 + \alpha_3 f_3 + \;\cdots\; + \alpha_n f_n \;,$$

to form an arbitrary vector V within the subspace. Here V is an image of n loops and the α_i's are scalar "brightness" coefficients of the individual loops. Within this linear space forming the

complete image, the images of the individual loops form an independent sub-set of basis elements. This is seen since the potential or other extrapolation methods of the field provides a one-to-one mapping of the foot points, i.e., the foot points form a unique pair of position coordinates (a positive B_z foot point and a negative B_z foot point), and no two identical images can be generated from a signal set of foot points, since all the other loops are either greater or lesser in extent across the specific neutral line in the same direction, providing for unique images. Of course, a necessary condition is that only one foot point for any of the loops is generated within an individual image pixel. No two loops can have the same image due to the unique foot point locations and the higher loops will also be more extended in width. In particular the image pixel size will place a limit on the number of independent loop images. However, this can be tested in the application to insure linear independency of the images by employing the Gramian condition (Hilderbrand 1952).

3.2 NON-NEGATIVE LEAST SQUARES METHOD

The inner product (f,g) in this space, $R^{m \times m}$-space, is the regular vector dot product and we can define the projection of f in the direction of ϕ by proj(f:ϕ)=(f,ϕ)ϕ, where $(\phi,\phi)^{1/2}$=1. Furthermore for an observed image h and given a set of defined flux-tube loop images, f_i's, we can define the sum

$$S_{um} = \left| h - \alpha\, f \right| = \left| h - \alpha_1 f_1 - \alpha_2 f_2 - \alpha_3 f_3 - \cdots - \alpha_n f_n \right| \qquad n \le m^2,$$

which assumes the minimum if we chose

$$\alpha_k = (h, f_k),$$

i.e., a least squares solution (Davis 1963) . This assumes that all the flux tubes are optically thin so that the images can be summed linearly. When the images do not form an orthogonal sub-space, we can still form the least squares solution subject to the constraint that all the α's are nonnegative, i.e., the images of the loops have only a positive contribution. For this purpose the Kuhn-Tucker conditions of the least squares solution are imposed. If f is the matrix formed by the n-column vectors of the images (m^2 elements) and α is the n-vector form by the α_i's, then the resulting Kuhn-Tucker theorem is then given as follows:

> An n-vector α is a solution of the least square solution of minimizing
> ||h-αf|| subject to the constraint $\alpha \ge 0$ if and only if there exists a k-vector
> $\mathbf{y}$ = (f, fα-h) and a partitioning of the integers 1 through k into the subsets
> $\mathcal{E}$ and $\mathcal{S}$ such that:

α_i=0 for $i \in \mathcal{E}$	α_i>0 for $i \in \mathcal{S}$
$y_i \ge 0$ for $i \in \mathcal{E}$	y_i=0 for $i \in \mathcal{S}$

(Lawson and Hanson 1974).

The derivation of the theorem uses the fact that the vector $\mathbf{y}$ = (f, fα-h) is the negative gradient vector of $1/2 \|f\alpha\text{-h}\|^2$ and is related finding the minimum of the norm. An appropriate FORTRAN computer algorithm is given by Lawson and Hanson (1974) for solving the constrained linear least square problem. The problem is one of searching along the negative gradient of the least square norm while keeping $\alpha \ge 0$. The problems of noise, under determinacy, and column degeneracies are handled by employing the property that one linearly independent column vector is added or removed at each step using QR decomposition methods in solving the multiple linear

regression equation h - α f = 0 for the various α's needed in the Lawson-Hanson algorithm. In the software developed, an IDL External_Call routine was used to employ the Lawson and Hanson algorithm directly.

3.3 PROCESS OVERVIEW

The overall set of programs is shown in the flow chart of Figure 6. For the data used in this paper, the KPNO longitudinal magnetogram used was obtained on 1994 Janurary 4 at 1631 UT. The FITS formatted 512×512 magnetogram with 4.88 ×4.88 arcsec pixels was used uncorrected for rotation and saturation. A 200×200 sub-image about the transequatorial active regions AR 7645 and AR 7646/47 was extracted. A *Yohkoh* SXT AlMg image taken on the same day at 0735 UT with 4.92×4.92 arcsec pixels was used. From the full disk FITS image, a sub-image was extracted, rescaled, and registered with the magnetogram. Both sub-images are then scaled up to a 400×400 pixel image to provide spatial resolution in the rendering analysis. Using this sub-image of the full magnetograph, a set of 290 potential field lines was generated using the line-of-sight, spherical model of Sakurai's potential code (Sakurai 1981) in which the foot point distribution is determined by the strength of the flux distribution. The field lines generated are viewed as from Earth and are imported into a program to render each field line that has both photospheric foot points within the field of view of the sub-image field of view. The short field lines with a total arclength <24 arcsec are also rejected from the analysis since they contribute very little to the overall image and interfere with the current codes' performance. A flux rendering program is used to produce an optically thin flux-tube image of each of the remaining field lines. Per computation pass, the rendering program assumes that each flux tube has a standard radius (e.g. 0.8 pixel) at the photosphere for the set of field lines. Starting at a foot print the voxels are determined by the nearest neighbor technique described above. Then each voxel within a flux tube is assigned an emission value of 1 and the values are summed along the line-of-sight direction, e.g. z-axis, to give a pseudo-image of the flux tube. A correction to the sum is applied so that the hydrostatic equilibrium scale height is taken into account. The correction is very small as we shall see. This is done for each flux tube and for each a separate image is obtained for each flux-tube loop (f_i's). Using the sub-image of the *Yohkoh* image (h) and the loop images (f_i's) we minimize || h-αf || using the Lawson-Hanson algorithm which maintains the constraint $\alpha \geq 0$, and obtain the brightness coefficients α_i for each flux tube of length L_i. Hence we obtain a corresponding image to the observed image with the given assumptions. We shall now give the specific results for the active regions investigated.

4. Results

4.1 SINGLE LOOP

Before we present the multi-loop configurations we present a single flux loop configuration. Figure 4 gives a single image of a rendered flux tube showing the flux tube in five different orientations. We will assume that any combination of flux-tube loops remain optically thin, hence this allows the linear combination of images to be valid. This allows the formation of complex images via a sum of single loop images. This simulates an unchanging flux tube rotating

from the east limb to the central meridian longitude. The emission properties of a single X-ray loop is simulated. On the limb the effect of the conservation of flux is seen in the expanding flux tube. As the flux tube is rotated the line-of-sight effects become more apparent. The line-of-sight effects are not very apparent on the limb in the case shown since the plane of the loop is perpendicular to the line of sight. On the limb the main line-of-sight effect is due to the thickness of the tube as the radius of the tube expands. When the flux tube is seen on the central meridian the line-of-sight effects of looking down through the legs of the tube are apparent. Hence the bright regions of the tube has shifted from the apex on the limb to the legs on the disk. Since the line of sight is not symmetric down both legs, one leg appears brighter. A photospheric field-strength difference would change the radius of the tube at the different foot points and could also cause a difference. In the last panel of Figure 4 we have the same loop shown except the effect of hydrostatic scale factor is not included. The loop height is 0.5×10^5 km and the scale height is 0.4176×10^5 km, typical of an isothermal corona of $T = 6.2 \times 10^6$K and a perfect gas.

4.2 MULTI-LOOP IMAGING BY SUMMATION

For a set of loops the combined image is just the sum of the individual loop images since we have assumed an optically thin plasma. This allows the linear superposition and provides a simple method of creating a combined image without having to have all the flux tubes in the z-buffer at the same time and doing a sum there. Figure 5 shows the results of a multi-loop imaging technique. This image begins to resemble an X-ray image for multi-loops. The contrast is much higher than the images from an X-ray telescope due to the background emission and the scattering in the instrument. Again the line-of-sight effects are clearly seen being produced by the width of the flux tube, the longitudinal views, and now the overlapping of flux tubes. One can see "loop top" brightenings as a consequence of loops overlapping in the field of view, and, of course, they have no relation with loop "interactions" in the physical sense. Such a geometric analysis will be important in understanding the reported findings of "coronal loop interactions" (CLIs), in which the brightening at two overlapping loops is reported as a physical effect (Airapetian and Smartt 1995, Smartt, Zhang, and Smotko 1993). It is clearly seen in the reconstructed images that the loop top brightenings can be due to a geometric effect; however the brightness could vary as a function of time if the density and/or temperature varies.

4.3 INVERSION SOLUTIONS

The inversion process will now be illustrated by taking a *Yohkoh* SXT image (Figure 1) and the flux tube that have been rendered into images and determining the appropriate brightness coefficients associated with each flux tube. Figures 7, 8 and 9 provide a set of images of the 1994 January 4 transequatorial active regions derived from the inversion process. A base radii of r_o= 0.25, 0.25 and 0.75 were used in the Figures 7, 8 and 9, respectively. The original SXT subimage

had 400×400 pixels (16.4×16.4 arcmin) for the region selected and there were 290 field lines used in the inversion process, with the reduction of field lines not closing within the field of view and the removal of very short field lines (s < 24 arcsec), the number of field lines was reduced to 187 with ~5% more rejected by the non-negative least squares inversion process.

In testing the inversion process the 400×400 images were averaged into smaller arrays, i.e. images of 20×20, 40×40, 80×80 and 200×200, to test the effect of the array size on the resulting pseudo-image and the brightness coefficient and, hence, to test the non-negative least squares method. As expected, the number of flux tubes used by the inversion process was reduced. For an increased average pixel size giving a 20×20 array, 46% field lines were deleted by the non-negative constraint, as compared to the 400×400 case.

A comparison of the resulting 400×400 pseudo image with the SXT image shows similarity in the brightness of the main active regions, the x-type neutral point between the active regions, and the same general field configuration. The high contrast on the pseudo-image is the first point of departure between the two images. An arbitrary diffuse emission can be introduced into the pseudo-image and the resulting contrast will match the observation much closer. The basis for such an introduction is not explored in this paper.

Since the field of view is more than 16×16 arcmin, we conjecture that most of the differences between the large, long flux-tube loops of the pseudo-image and the observations are mainly due to the effect of a source surface which would affect the longest, highest field lines the most (e.g., Poletto and Kopp 1988). This effect will be studied in a later paper. Other effects might be the field lines selected and hence related to the number of field lines used. An increase in the number of field lines would allow the rendered flux tubes to span the image space more effectively.

4.4 SCALING LAW RESULTS

In order to show the usefulness of this approach in determining physical parameters of the flux tubes we investigate the brightness coefficients in connection with the scaling laws. The analysis by Kano and Tsuneta (1995) of observations by SXT in terms of the scaling laws support, in part, the early *Skylab* results by Rosner, Tucker and Vaiana (1978); however these later observations include transient brightenings and resulted in a revised scaling law. Furthermore, the analysis by Yoshida and Tsuneta (1996) provides data on the structure of the temperature and density variation across active regions; the SXT image "can serve as pressure and density maps". The results of our image analysis relate directly to these papers. In Figure 10 the relationship between the brightness coefficients and the loop lengths is given along with reference curves which plot $I=L^{-2}$. An individual data point is derived from the brightness coefficients (via section 5.2) for a specific flux tube and hence a specific length as given by the potential field extrapolation. Using the scaling laws, emission per unit volume is $j_\lambda \sim L^{-2} T^{-7/2}$, if we relate this directly to brightness of the loops we obtain the set of references curve given in Figure 10. Hence for a given maximum temperature, the emission should be defined by an L^{-2} curve. The variation of temperature from loop to loop should change by a factor of less than 4, i.e., 2 MK

to 8 MK; and then the maximum change in brightness as the result of temperature changes could be a factor of ~100. The other variation in the scatter plot can come from (1) partial contributions from multi-loops, (2) the natural spread in the scaling laws, (3) transient loops which follow different scaling laws, (4) temperature variations, and (5) temperature sensitivity effects of SXT. Here we have shown the results are consistent with the scaling laws. The derivation of the specific scaling laws requires the inclusion of a detailed physical component which would be more complete than the isothermal assumption made herein. If we fix L, the brightness is a function of $T^{-7/2}$ and we can use the relationship to determine T, if we can eliminate the diffuse background component.

5. Conclusion

We have given the theoretical and numerical treatment of a unique method for rendering plasma flux-tube emission in soft X-rays. A potential extrapolation method has been employed along with an isothermal corona. This was initiated to show the usefulness of the method and more complex cases can now be considered in terms of the extrapolation field and the physical assumptions concerning the flux tubes. The imaging method does converge as a function of the brightness coefficients since the non-negative least squares is a stable process. This paper is an exploratory paper using standard techniques in terms of simple models. It produces images very consistent with observations in terms of both the linear features and the physical scaling laws. The findings imply that further work in this area will provide a useful tool for understanding the 3D structure of the corona and the strengths and weaknesses of the scaling laws. Further development to be pursued includes using (1) field-lines extrapolations to define the flux tube, instead of using the conservation of flux and circular cross sections, (2) more complex field configurations, e.g., source surface potential models and force-free magnetic field models, (3) actual scaling laws for non-isothermal models, (4) actual thermal spectrum and instrument response functions, (5) unsaturated magnetograms, and (6) expanded mathematical, physical, and computer algorithms.

References

Airapetian, V. S., and Smartt, R. N.:1995, *Astrophys. J.* **445**, 489.

Alexander, D., and Katsev, S.: 1996, *Solar Phys.*, **167**,153.

Bray, R. J., Cram, L. E., Durrant, C. J., and Loughhead, R. E.: 1991, *Plasma Loops in the Solar Corona*, Cambridge University, Cambridge.

Culhane, J. L.: 1969, *Monthly Notices Roy. Astron. Soc.* **144**, 379.

Ciaravella, A., Peres, G., Maggio, A., and Serio, S.: 1996, *Astron. Astrphys.* **306**, 553.

Davis, H. F.: 1963, *Fourier Series and Orthogonal Functions*, Allyn and Bacon, Boston, Ch. 2, p. 52.

Démoulin, P., van Driel-Geszfelyi, Schmiedder, B., Hénoux, J. C., Csepura, G., and Hagyard, M. J.: 1993, *Astron. Astrophys.* **271**, 292.

Démoulin, P., Mandrini, C. H., Rovira, M. G., Hénoux, J. C., and Machado, M. E.: 1994, *Solar Phys.* **150**, 221.

Drebin, R. A., Carpenter, L., and Hanrahan, P.: 1988, *Computer Graphics* **22**, 65.

Elwert, G.: 1961, *J. Geophys. Res.* **66**, 391.

Fox, P.: 1908, *Astrophys. J.*., 28, 253.

Gary, G. A.: 1992, *Mem. Soc. Astr. Italy* **61**, 457.

Gibson, E. G.: 1973, *The Quiet Sun*, NASA SP-303, p. 295.

Godovnikov, N. V., and Smirnova, E. P.: 1965, *Izv. Kyrm. Astrophys. Obs.* **33**, 86

Hagyard, M. J.: 1988, *Solar Phys.* **115**, 167.

Hagyard, M. J.: 1990, *Mem. S. A. It.* **61**, 337.

Harvey, J.W.: 1966, *Evaluation of Solar Magnetograms*, Astro-Geophysical Memorandum No. 2, High Altitude Observatory, Boulder, Colorado.

Harvey, J. W.: 1969, Ph. D. thesis, Univ. Colorado.

Hilderbrand, F. B.: 1952, *Methods of Applied Mathematics*, Englewood: Prentice-Hall, p. 25.

Hoyng, P. and 23 co-authors: 1981, *Astrophys. J.* **244**, L153.

Kano, R., and Tsuneta, S.: 1995, *Astrophys. J.* **454**, 934.

Kaufman, A.: 1987, *Computer Graphics* **21**,191.

Klimchuk, J. D.: 1995, *Bull. AAS* **27**, 996.

Klimchuk, J., Lemen, J., Feldman, U., Tsuneta, S., and Uchida, Y.: 1992, *Publ. Astron. Soc. Japan* **44**, L181.

Lang, K.R.: 1980, *Astrophysical Formulae*, Springer-Verlag, New York, p. 46 and p. 456.

Lawson, C. L., and Hanson, R. J.: 1974, *Solving Least Squares Problems,* Prentice-Hall, Englewood Cliffs, p. 58.

Levine, R. H.: 1975, *Solar Phys.* **44**, 365.

Levine, R. H.: 1976, *Solar Phys.* **46**, 159.

Levine, R. H., and Altschuler, M: 1977, *Solar Phys.* **36**, 345.

Levine, R. H.: 1982, *Solar Phys. 79,* 203.

Maggio, A, and Peres, G.: 1996, *Astron. Astrophys.* **306**, 563.

McClymont, A. N., and Mikic, Z.: 1994, *Astrophys. J.* **422**, 899.

Mewe, R., Gronenschild, E. H. B. M., and van der Oord, G. H. J.: 1985, *Astron. Astrophys. Suppl. Ser.* **63**, 195.

Mewe, R., Lemen, J. R. and van der Oord, G. H. J.: 1986, *Astron. Astrophys. Suppl. Ser.* **65**, 511.

Mikic, Z., Barnes, D. C., and Schnack, D. D.: 1988, *Astrophys. J.* **328**, 830.

Mikic, Z., Schnack, D. D., and Van Hoven, G.: 1989, *Astrophys. J.* **338**, 1148.

Mikic, Z., Schnack, D. D., and Van Hoven, G.: 1990, *Astrophys. J.* **361**, 690.

Mikic, Z. and McClymont, A. N.: 1994, in K. S. Balasubramaniam and G. Simon (eds.), *Solar Active Region Evolution,* ASP Conf. Ser. **68**, 240.

Moore, R. L., Hagyard, M. J., and Davis, J. M.: 1987, *Solar Phys.* **113**, 347.

Nakagawa, Y.: 1973, *Astro. Ap.* **27**, 95.

Nakagawa, Y., and Raadu, M. A.: 1972, *Solar Phys.* **25**, 127.

Nakagawa, Y., Raadu, M. A., Billings, D. E., and McNamara, D.: 1971, *Solar Phys.* **19**, 72.

Parker, E. N.: 1979, *Cosmical Magnetic Fields*, Clarendon Press, Oxford, p.123.

Priest, E. R.: 1982, *Solar Magnetohydrodynamics,* Reidel, Dordrecht, Holland, p. 108).

Poletto, G., Vaiana, G. S., Zinbeck, M. V., Kriege, A. S., and Timotym A. F.: 1975, *Solar Phys.* **44**, 83.

Poletto, G., and Kopp, R. A.:1988, *Solar Phys.* **116**, 163.

Raadu, M. A., and Nakagawa, Y.: 1971, *Solar Phys.* **20**, 64.

Reale, F., and Peres, G.: 1995, *Astron. Astrophys.* **299**, 225.

Rosner, R., Tucker, W. H., and Vaiana, G. S.: 1978, *Astrophys. J..* **220**, 643.

Roumeliotis, G.: 1994, in K. S. Balasubramaniam and G. Simon (eds.), *Solar Active Region Evolution,* ASP Conf. Ser. **68**, 240.

Rust, D. M.: 1966 Thesis, University of Colorado.

Rust, D. M.: 1970, *AIAA Observations and Predictions of Solar Activity Conf.*, Huntsville, AL).

Rust, D. M., and Roy, J.-R.: 1971, in R. Howard (ed.), *Solar Magnetic Fields*, IAU Symp. 43, Reidel, Dordrecht, Holland, p. 569.

Sakurai, T.: 1981, *Solar Phys.* **69**, 343.

Sakurai, T.: 1982, *Solar Phys.* **76**, 301.

Serio, S., Peres, G., Vaiana, G. S., Golub, L, and Rosner, R.: 1981, *Astrophys. J.* **243**, 288.

Schmidt, H. U.: 1965, *Mitt. Astron. Ges.*, Sept, 89.

Schmidt, H. U.: 1964, in W. N. Ness (ed.), *Solar Flares,* AAS-NASA Symp., NASA SP-50, p.107.

Semel, M.: 1967, *Ann. Astrophys.* **30**, 513.

Sheeley, N. R., Jr., Bohlin, J. D., Brueckner, G. E., Purcell, J. D., Scherrer, V., and Tousey, R.: 1975, *Solar Phys.* **40**, 103.

Shimizu, T.: 1994, in *New Look at the Sun with Emphasis on Advance Observations of Coronal Dynamics and Flares,* ed. S. Enome and T. Hirayama, (Nagano: Nobeyama Radio Observatory), p. 61.

Shimizu, T., Tsuneta, S., Action, L., Lemen, J., Ogawara, Y., and Uchida, Y.: 1994, *Astrophys. J.* **422**, 906.

Smartt, R., Zhang, Z., and Smotko, M. F.: 1993, *Solar Phys.* **148**, 139.

Somov, B. V.: 1992, Physical Processes in Solar Flares, Kluwer Acad. Pub., Boston, p.15

Tsuneta, S. 1996, *Astrophys. J. Letters* **456**, L63.

Wang, H.: 1992, *Solar Phys.* **140**, 85.

Webb, D. F.: 1981, in *Solar Active Resions, Skylab Solar Workshop III,* ed. F. Q. Orrall, Colorado Assoc. Press, Boulder, p. 165.

Wellck, R. E., and Nakagawa, Y.: 1973, *NCAR Tech. Note TN/STR-87*, NCAR, Boulder, CO.

Wu, S. T, Chang, H. M., and Hagyard, M. J.: 1985, in M. J. Hagyard (ed.) in *Measurements of Solar Vector Magnetic Fields*, NASA CP-2374, p.17.

Wu, S. T., Sun, M. T., Chang, H. M., Hagyard, M. J., and Gary, G. A.: 1990, *Astrophys, J.* **362**, 698.

Wu, S. T., and Sakurai, T.: 1990, *Mem. S. A. It.* **62**, 477.

Yoshida, T., and Ogama, Y.: 1995, *Publ. Astron. Soc. Japan* **47**, L15.

Yoshida, T., and Tsuneta, S.: 1996, *Astrophys. J.* **495**, 342.

Yoshida, T., Tsuneta, S., Golub, L., Strong, K., and Ogawara, Y.: 1995 *Publ. Astron. Soc. Japan* **47**, L15.

Figures Captions

Figure 1. Transequatorial Active Region 7645 and 7646/7647 on 1994 January 4. (a) *Yohkoh* SXT image (0735UT) shows the associated 3-6×10^6K degree X-ray emission as obtained by the AlMg filter, (b) KPNO magnetogram (1631UT) shows the associated longitudinal magnetic field in the region of 16×16 arcmin, (c) the magnetic field lines generated by Sakurai's spherical potential code is shown as viewed from Earth, (d) the same magnetic field lines as in(c) are shown in profile. No source surface is employed as is apparent in the profile view.
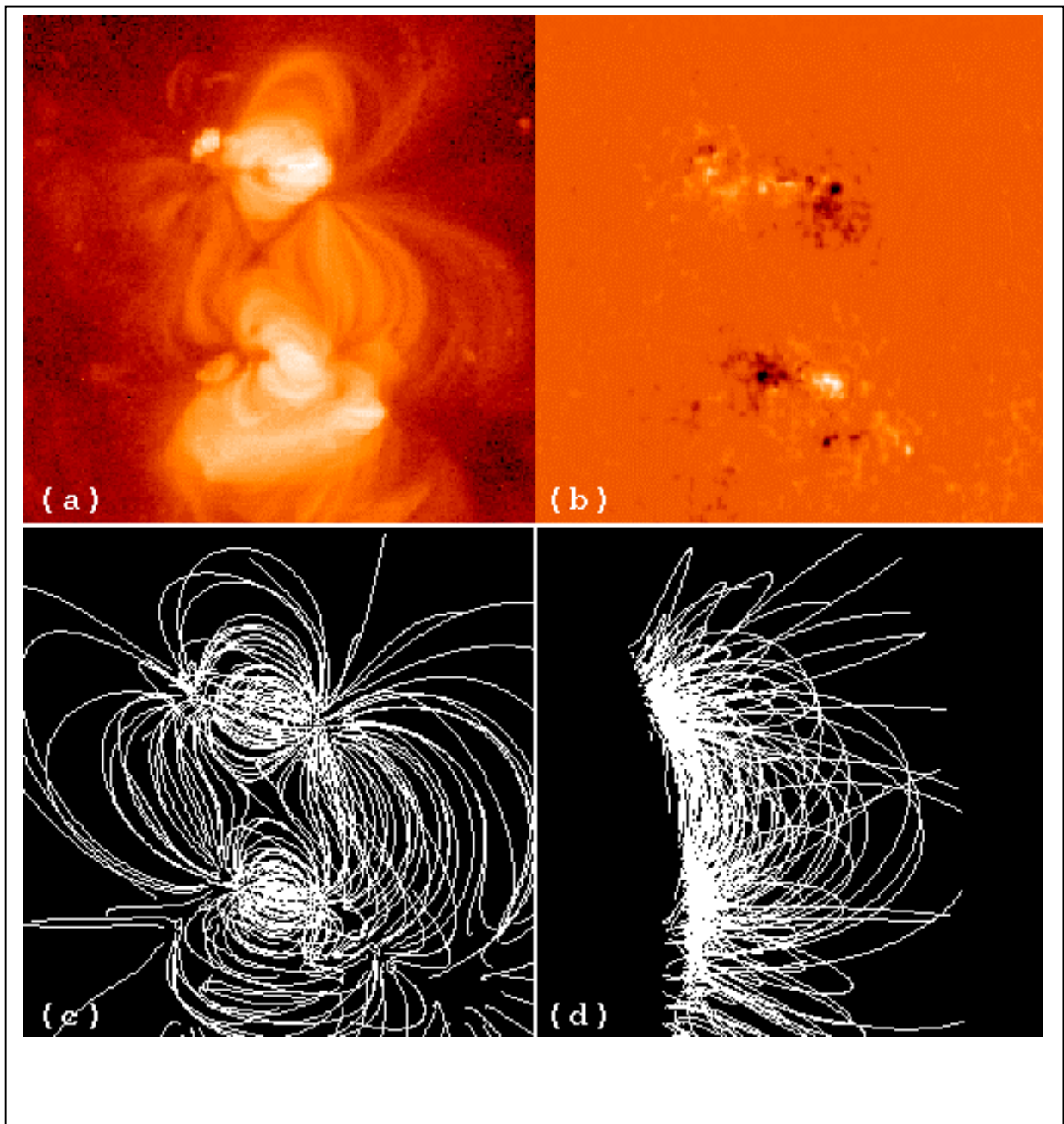
Figure 2. Potential Flux-Tube Characteristics. (a) The normalized ratio R of the cross sectional radii vs normalized arclength (L) along the loop from the apex is plotted. Only one side of each loop is used. The shorter field lines have a higher R value at a normalized arclength of L=1, i.e., the short loops have a smaller change in the field strength along the loop. (b) The reciprocal normalized flux ratio R^{-1} of the cross sectional radii vs the arclength from the apex measured in Mm is plotted.
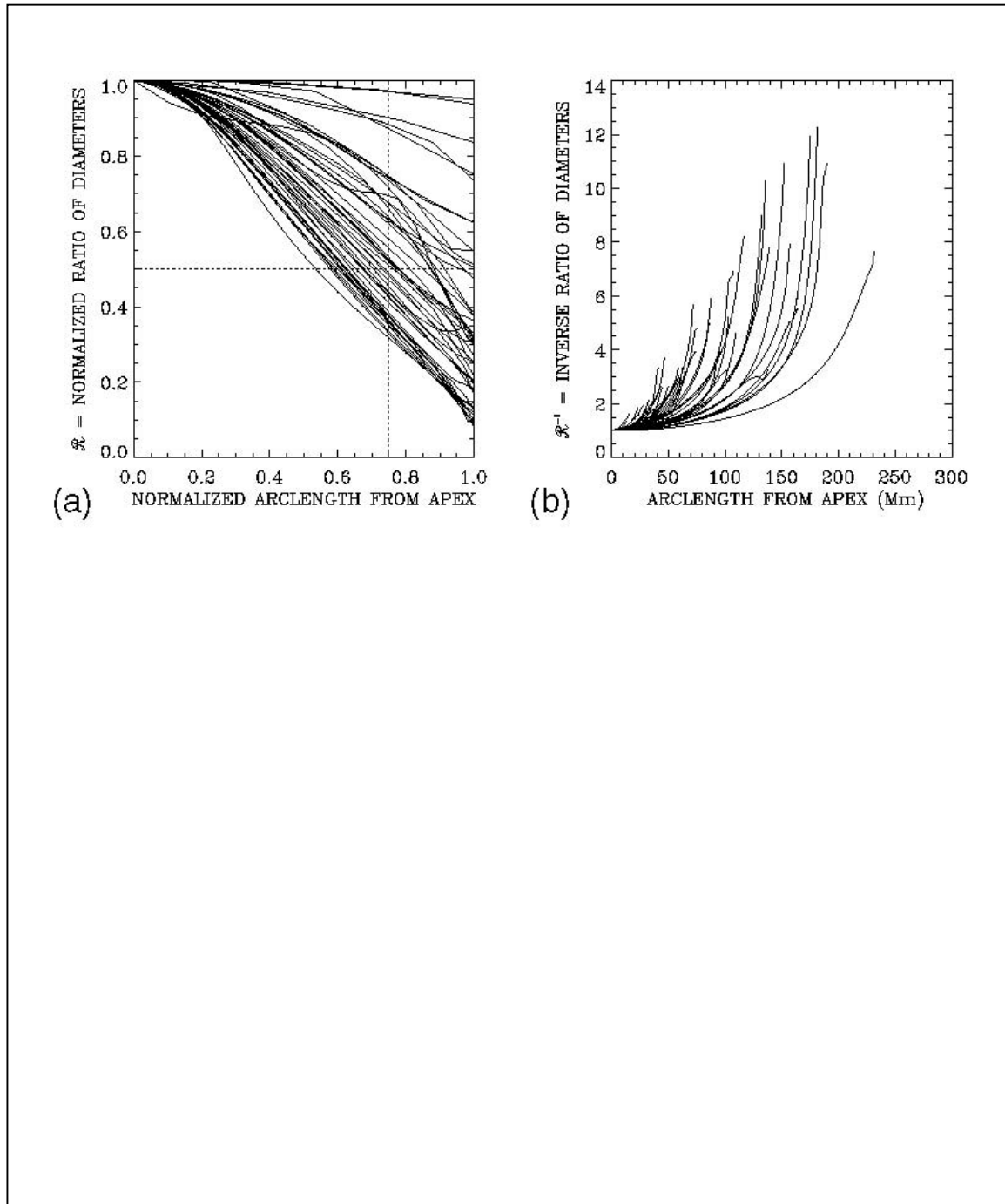
Figure 3. Solid Flux Tubes Displayed for the Active Regions 7645 and 7646/7647. Only the outer surface of the flux tubes are shown. The expansion of the flux tube is displayed, with the highest flux tubes having the largest radii. The field lines used in generating this plot are the same as Figure 1c and 1d. The same initial photospheric radius is constant all the flux tubes (4 arcsec). The changes in the radius of the flux tubes are due only to the change in the magnetic field.
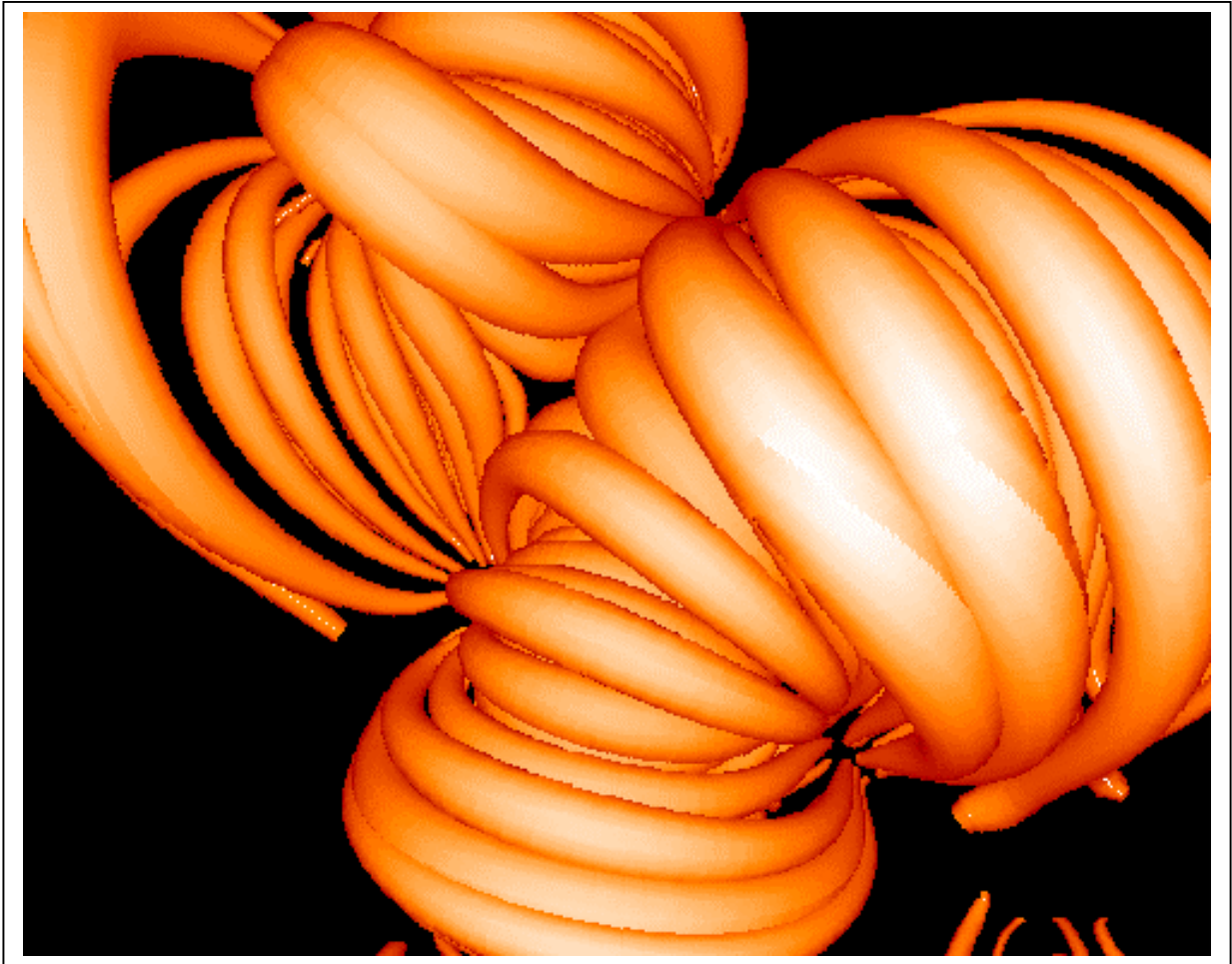
Figure 4. Single Plasma Flux Rendering. (a-e) A flux tube is seen as it would appear rotating onto the sun's disk in a series of images from the eastern limb to disk center in 5 steps with north up. The different line-of-sight effects are seen.   In the last panel (f), the same disk center image of (e) is given for the flux tube except without the hydrostatic corrections. The images were composed of 400×400 pixels using potential field lines from Figure 1.
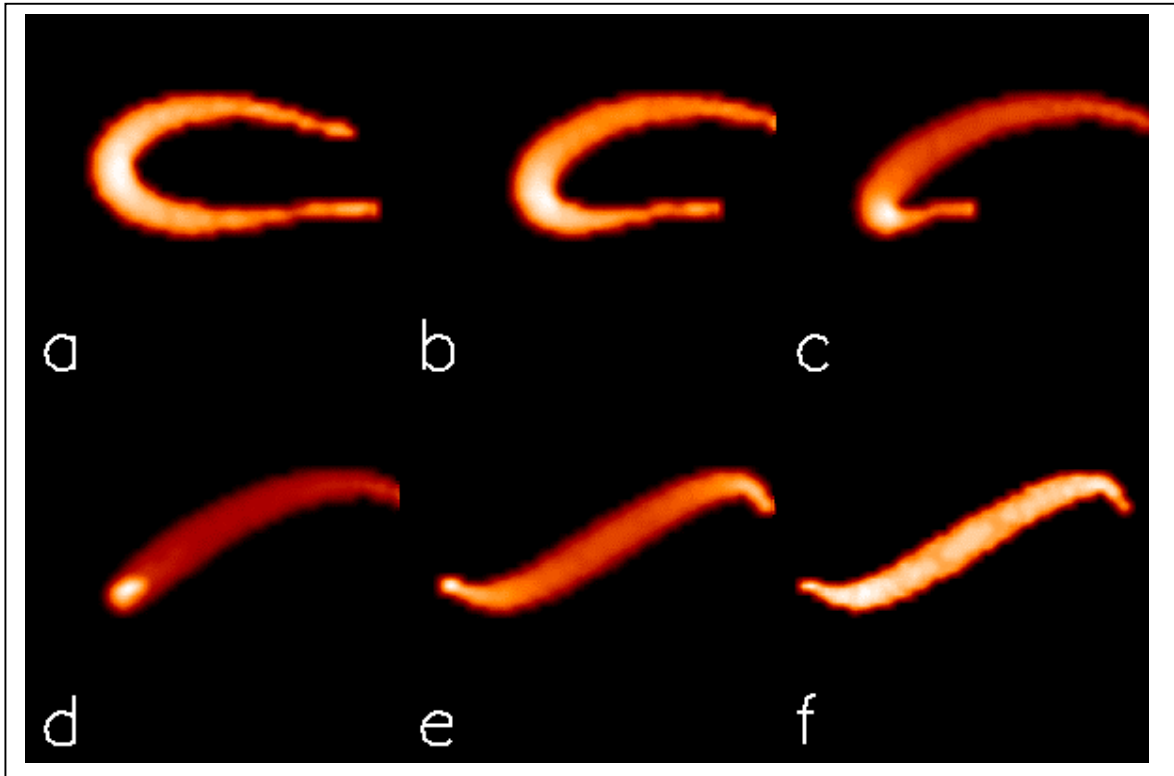
Figure 5. Multi-Flux-Tube Rendering. (a-e) A series flux tubes with the hydrostatic correction is seen as it would appear rotating onto the sun's disk as per Figure 4. The line-of-sight effects of over-lapping images are seen. On the limb the main effect is enhanced loop top brightening. On the disk center the location and strength of the brightening change as the aspect angle is changed. In the last panel (f), the same disk center orientation of (e) is given for the flux tube except without the hydrostatic corrections.
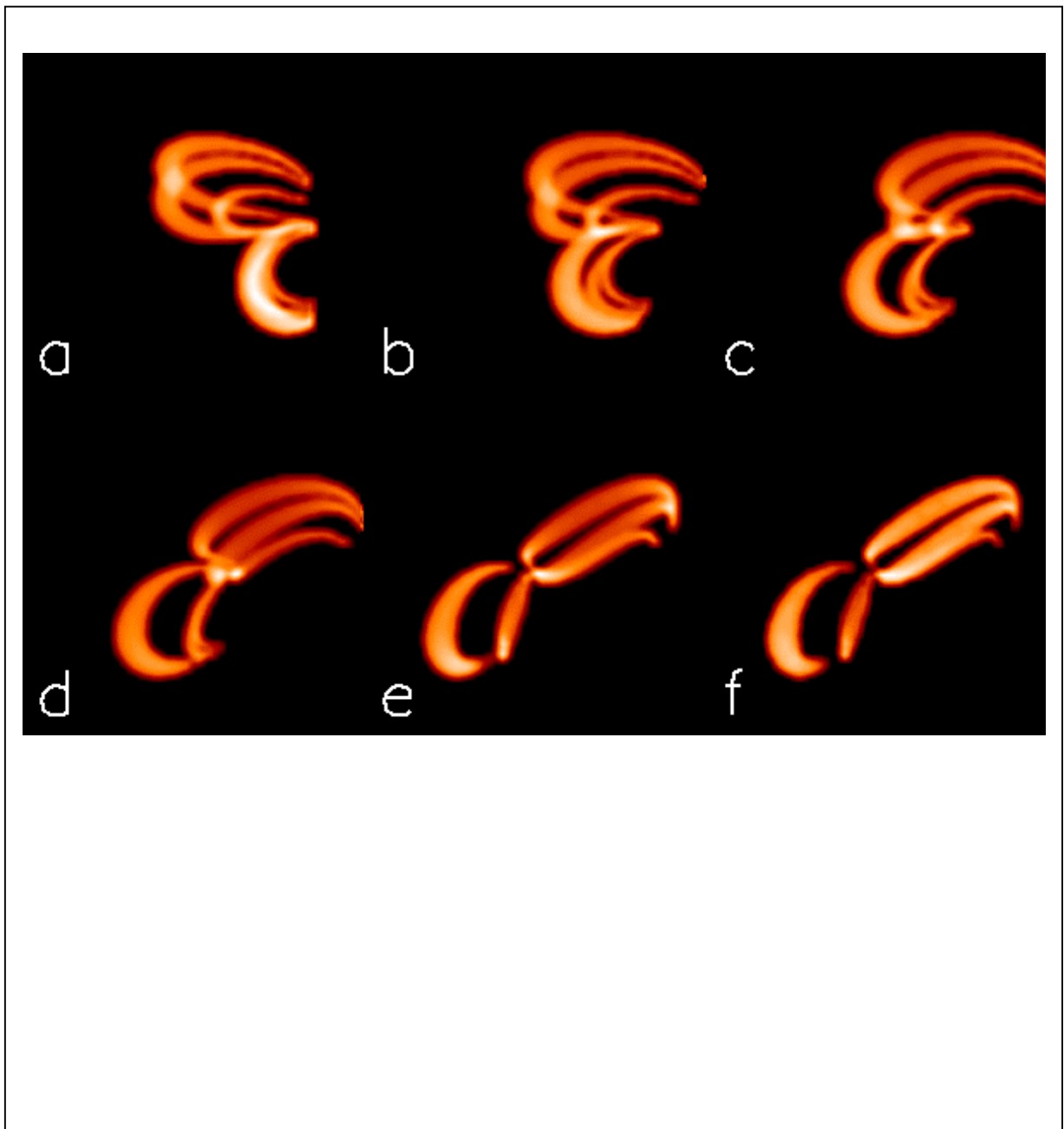
Figure 6. A Flow Chart of the Inversion Technique. A Yohkoh image is extracted and field lines are generated from a magnetogram. Then each field line is rendered into a flux tube. This set of individual images of coronal flux tubes (f_i) is summed to form a pseudo-image of soft X-ray emission. The individual image coefficients (α_i) are determined by minimizing


3D Flux–Tube Rendering Program
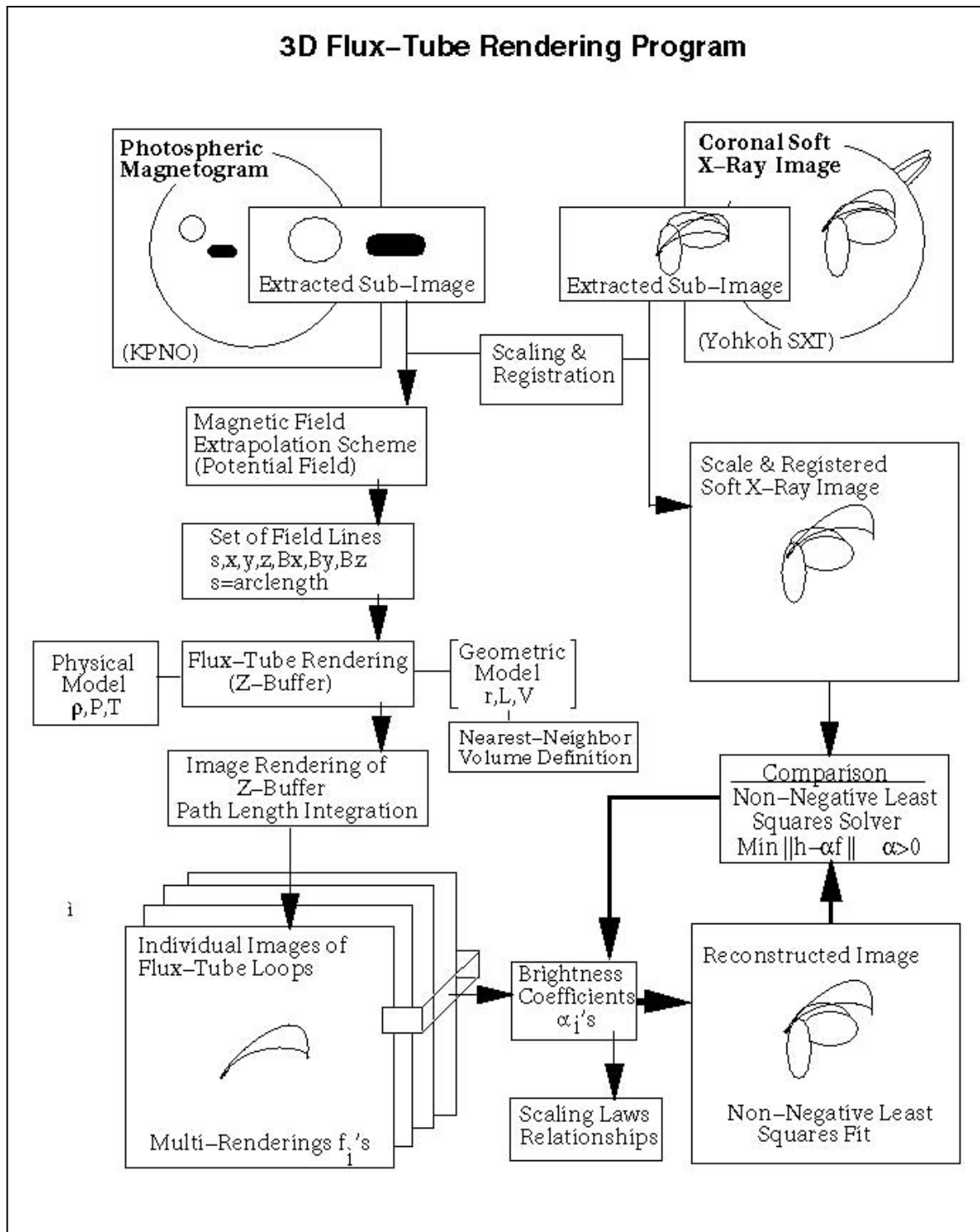
difference $\|h-\alpha f\|^2$ between the pseudo-image (αf) and the observed soft X-ray image (h).

Figure 7. Comparison of the Resulting Image and *Yohkoh* SXT Images with a Base Radius fixed at r_0=0.25. The differences seen arise from the high contrast resulting from not having a diffuse component in the analysis and the narrow flux tubes resulting from the given base radius. The differences in some of the large linear features may be due to a number of
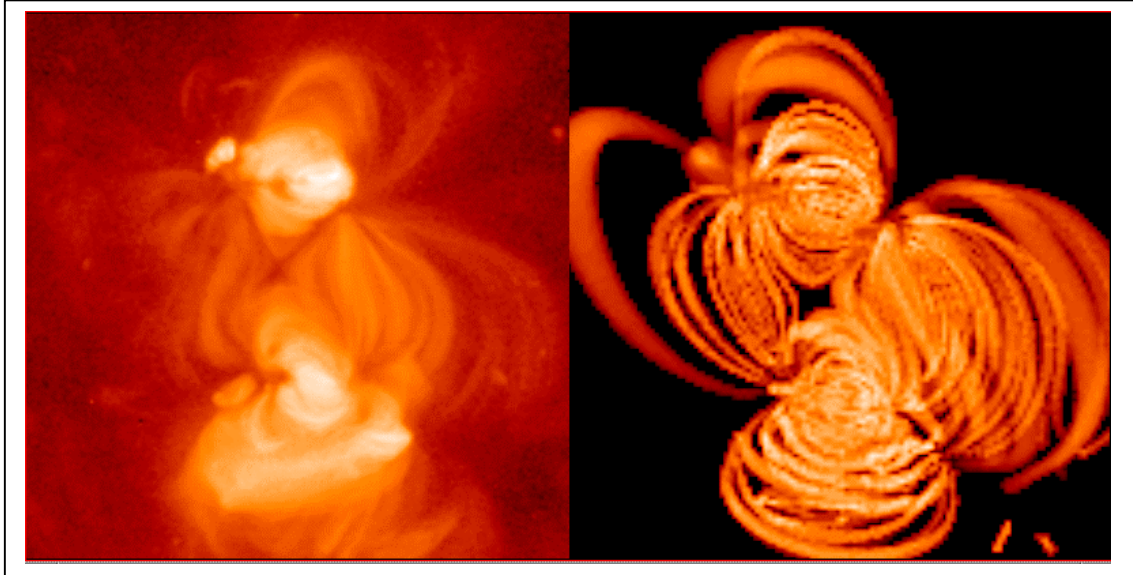
effects listed in the text.

Figure 8. Comparison of the Resulting Image and *Yohkoh* SXT Images with a Base Radius fixed at r_0=0.50. The expanded loops configuration gives an image with striking similarities in terms of the overall linear structures and the location of the x-type neutral point,
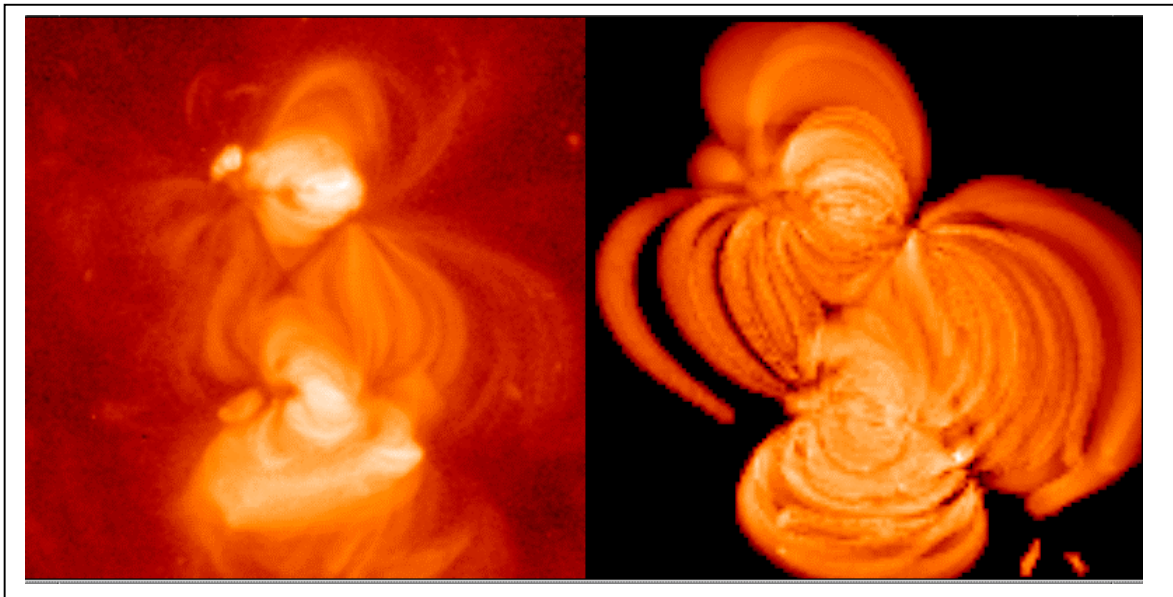
especially under the assumption of a potential configuration and an isothermal environment

Figure 9. Comparison of the Resulting Image and *Yohkoh* SXT Images with a Base Radius fixed at $r_0=0.75$. The x-type neutral point has been filled in be the expanding loops.
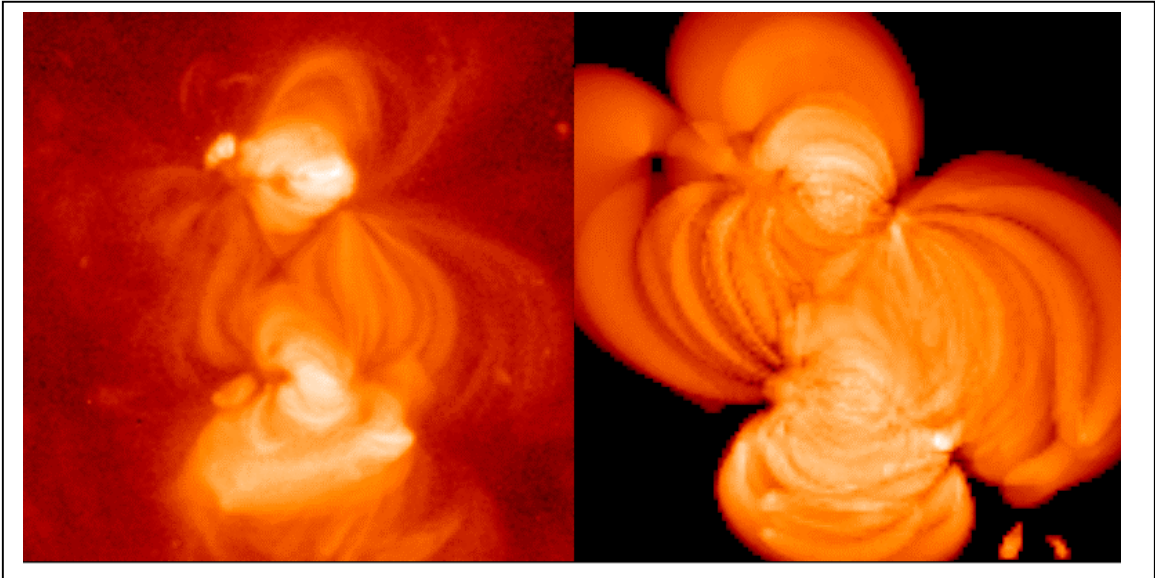
Figure 10. Scatter Plot of Brightness Coefficients vs Arclength. The relationship between the brightness coefficients and the loop lengths is given along with reference curves which plot $I=L^{-2}$ which indicate the consistency with the RTV scaling laws.